

# Analysis and Comparison of Peak-to-Peak Current Ripple in Two-Level and Multilevel PWM Inverters

Gabriele Grandi, *Senior Member, IEEE*, Jelena Loncarski, *Student Member, IEEE*,  
Obrad Dordevic, *Member, IEEE*

**Abstract**—Three-phase multilevel inverters are used in many medium- and high-power applications such as motor drives and grid-connected systems. Despite numerous PWM techniques for multilevel inverters have been developed, the impact of these modulation schemes on the peak-to-peak output current ripple amplitude has not been addressed yet. In this paper the analysis and the comparison of current ripple for two- and three-level voltage source inverters are given. Reference is made to optimal and popular modulation, so-called centered PWM, easily obtained by both carrier-based modulation (phase disposition, with proper common-mode voltage injection) and space vector modulation (nearest three vectors). It is shown that the peak-to-peak current ripple amplitude in three-level inverters can be determined on the basis of the ripple in two-level inverters, obtaining the same results as by directly analyzing the output voltage waveforms of the three-level inverters. This procedure can be readily extended to higher level numbers. The proposed analytical developments are verified by both numerical simulations and experimental tests.

**Index Terms**—Multilevel inverters; three-level inverter; output current ripple; carrier-based PWM; space vector PWM.

## I. INTRODUCTION

THREE-PHASE two-level (2L) inverters are widely utilized in ac motor drives and in general for grid-connected applications. In last decades, multilevel (ML) inverters became more and more popular, due to improved output voltage waveforms and increased power ratings. In particular, the ML structure is capable of reaching high output voltage amplitudes by using standard power switches with limited voltage ratings.

Simple and reliable implementations of ML inverters are the cascaded connection of single-phase inverters (H-bridge) and the neutral point clamped (NPC) configuration. Among ML inverters, three-level (3L) are a viable solution for many high-power applications, both grid-connected and motor-load.

Since the performance of an inverter mainly depends on its modulation strategy, many PWM techniques have been developed in last decades for 2L and ML inverters [1]-[13]. Generally, these modulation techniques can be classified in two categories: carrier-based (CB) and space-vector (SV) modulation. It has been proved that phase disposition (PD)

carrier-based modulation and nearest three vectors (NTV) space vector modulation for 2L and ML inverters can be equivalent [4], [9]-[12]. In particular, PD CB-PWM leads to the same output voltages as the SV-PWM if a proper common-mode voltage is injected into the modulating signals. On the other hand, CB-PWM can be equivalently realized by NTV SV-PWM through a proper sharing of dwell times among the redundant switching states. Specifically, the nearly-optimal modulation so-called centered PWM (CPWM) is obtained by sharing dwell times among the redundant switching states, offering reduced harmonic distortion in output currents [4], [9]-[13].

The impact and the comparison of CPWM schemes on the peak-to-peak output current ripple amplitude in 2L and ML inverters has not been addressed yet. In [14] the current ripple trajectory in  $\alpha$ - $\beta$  coordinates for the case of dual-inverter-fed open-end winding load configuration, operating as a 3L inverter is shown. However, emphasis was made to current ripple RMS rather than to the instantaneous ripple. The evaluation of peak-to-peak current ripple for 2L three-phase PWM inverters was first briefly introduced in [15] and better developed in [16]. A similar procedure has been proposed in [17], with further developments and insights but without experimental verifications. The same analysis has been extended to multiphase inverters in [18]-[21].

In general, for both 2L and ML inverters, the peak-to-peak current ripple distribution is useful to determine multiple zero-crossing intervals of the output current and the corresponding dead-time output voltage distortion [22]. Furthermore, the knowledge of current ripple amplitude can be used to compare PWM and hysteresis current controllers [23]-[25] and to define variable switching frequency PWM techniques [26].

This paper gives the evaluation and the comparison of the output current ripple amplitude in 2L and ML inverters. It is shown that the peak-to-peak current ripple amplitude in 3L and ML inverters can be obtained on the basis of the ripple evaluation in 2L inverters (which has been already addressed in the literature), by introducing the known concept of pivot voltage vector in 3L and ML case instead of null voltage vector in 2L case [27]. It is also shown that the results obtained with this method are the same compared with the results obtained directly by analyzing the output voltage waveforms of the 3L inverter. The peak-to-peak ripple amplitude is introduced as a function of the modulation index over a fundamental period, considering centered PWM switching patterns obtained either by CB- or SV-PWM techniques [11]-[13]. The instantaneous

Gabriele Grandi is with Department of Electrical, Electronic, and Information Engineering, University of Bologna, Italy (phone: +39-051-20-93571; fax: +39-051-20-93588; e-mail: gabriele.grandi@unibo.it).

Jelena Loncarski is with Department of Engineering Sciences, Ångström Laboratory, Uppsala University, Sweden (e-mail: jelena.loncarski@angstrom.uu.se).

Obrad Dordevic is with School of Engineering, Liverpool John Moores University, Byrom Street, Liverpool L3 3AF, UK (e-mail: O.Dordevic@ljmu.ac.uk).

current ripple is determined for a generic balanced three-phase load consisting of series RL impedance and ac back emf (RLE-load), representing both motor-load and grid-connected applications. The ripple analysis is verified by both numerical simulations and experimental tests in case of both 2L and 3L inverters, for different modulation indexes in the linear modulation range.

## II. SPACE VECTOR ANALYSIS AND PWM EQUATIONS

The use of space vectors in the analysis of 2L and ML three-phase inverters is introduced here since it leads to better understanding and more simple calculation of voltage levels and corresponding application times. The switching states of the  $k$ -th inverter phase can be denoted as  $S_k = [0, 1]$  for 2L inverter, and  $S_k = [-1, 0, 1]$ , *i.e.*  $\{-0+\}$  for 3L inverter. Further coefficients can be introduced for higher level numbers [7]-[8]. In this way, the output voltage vector  $\mathbf{v}$  of 2L and ML inverter can be expressed by

$$\mathbf{v} = \frac{2}{3}V_{dc} [S_1 + S_2\alpha + S_3\alpha^2] \quad (1)$$

being  $V_{dc}$  the dc supply voltage and  $\alpha = \exp(j2\pi/3)$ .

Fig. 1 shows the output voltage space vectors corresponding to all possible switch configurations in 2L and 3L inverters (Figs. 1a and 1b, respectively). For both inverters the space vector diagram appears to be a hexagon divided into six main triangles, sectors I–VI. Note that by supplying each multilevel cell of the 3L inverter with the same dc voltage of the 2L inverter, the resulting hexagon size is doubled, corresponding to double output voltage capability for the 3L inverter.

In addition to the redundant states corresponding to the null vector, there are six further redundant states corresponding to vertexes of inner hexagon, called pivot (or base) states in 3L inverter [27]. SV-PWM scheme uses the NTV algorithm to approximate the reference output voltage vector. In the case of continuous modulation strategies, the switching sequence starts from one pivot state, goes to the other switching states, and comes back to the first. Beginning and ending states of this traverse correspond to the same pivot (base) vector, that is the null vector in case of 2L inverters, and one of the six small

TABLE I  
SWITCH CONFIGURATION DUTY CYCLES FOR 2L AND 3L INVERTERS

2L inverter			
	$\delta_1$	$\delta_2$	$\delta_0$
I	$\frac{3}{2}(u_\alpha - 1/\sqrt{3}u_\beta)$	$\sqrt{3}u_\beta$	$1 - \frac{3}{2}(u_\alpha + 1/\sqrt{3}u_\beta)$
II	$\frac{3}{2}(u_\alpha + 1/\sqrt{3}u_\beta)$	$\frac{3}{2}(1/\sqrt{3}u_\beta - u_\alpha)$	$1 - \sqrt{3}u_\beta$
3L inverter			
	$\delta_1$	$\delta_2$	$\delta_p$
I-3b	$\frac{3}{2}(u'_\alpha - 1/\sqrt{3}u'_\beta)$	$\sqrt{3}u'_\beta - 1$	$2 - \frac{3}{2}(u'_\alpha + 1/\sqrt{3}u'_\beta)$
II-3a	$\frac{3}{2}(u'_\alpha + 1/\sqrt{3}u'_\beta) - 1$	$\frac{3}{2}(1/\sqrt{3}u'_\beta - u'_\alpha)$	$2 - \sqrt{3}u'_\beta$

vectors (magnitude  $2/3 V_{dc}$ ) in case of 3L inverters ( $\mathbf{v}_p$ , enlarged red dots in Fig. 1). This modulation principle can be extended to any ML inverter by a proper identification of NTV [7]-[8].

The working domain of each pivot vector is the sub-hexagon centered on it. In the case of 3L inverter it is restricted to a diamond-shaped region (pivot sector, pink colored area in Fig. 1 for  $\mathbf{v}_{p1}$ ), due to the overlaps between sub-hexagons.

For sinusoidal balanced output voltages, the reference output voltage vector is  $\mathbf{v}^* = V^* \exp(j\vartheta)$ , being  $V^* = m V_{dc}$ ,  $\vartheta = \omega t$ . Note that the limits of modulation index  $m$  are  $0 \leq m \leq 1/\sqrt{3}$  for 2L inverter and  $0 \leq m \leq 2/\sqrt{3}$  for 3L inverter. The analysis can be restricted to the first quadrant in the considered case of quarter-wave symmetric SV modulation.

The SV modulation of 3L and ML inverter can be traced back to the one of 2L inverter by considering the reference voltage  $\mathbf{v}^*$  as the combination of pivot voltage  $\mathbf{v}_p$  and residual 2L reference voltage  $\mathbf{v}_{2L}$ , for each pivot sector (Fig. 1c).

Application times  $t_k$  of NTV are defined by duty-cycles  $\delta_1$ ,  $\delta_2$ , and  $\delta_0$  *i.e.*  $\delta_p$ , for 2L *i.e.* 3L inverters, and switching period  $T_s$ , being  $\delta_k = t_k/(T_s/2)$ . Duty-cycles for the 1<sup>st</sup> quadrant of 2L inverter and corresponding quadrant of pivot vector  $\mathbf{v}_{p1}$  for 3L inverter (Fig. 2) are given in Table I. Normalized reference voltages  $u_\alpha$  and  $u_\beta$  used in Table I are defined as:

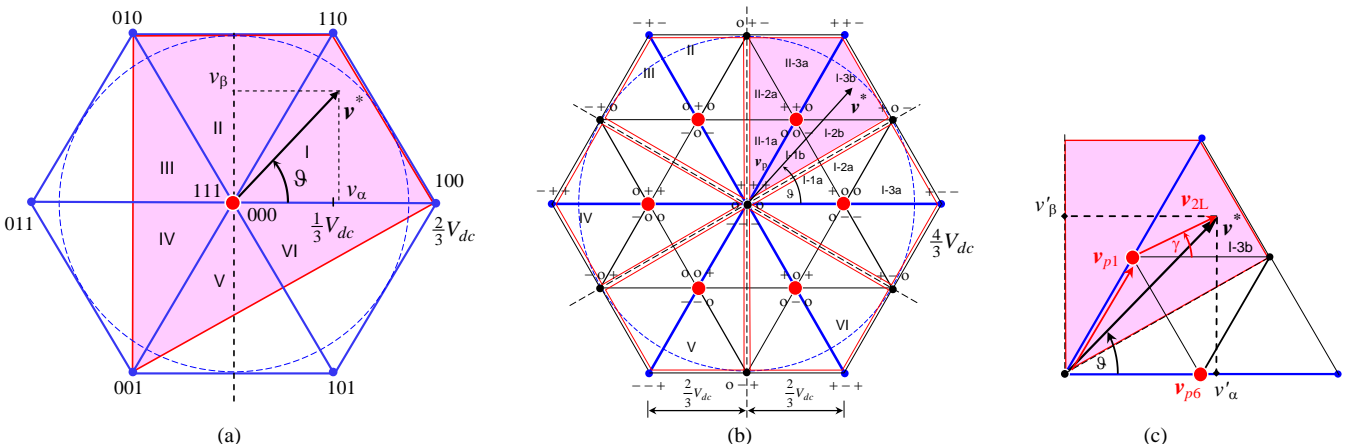


Fig. 1. Space vector diagrams of inverter output voltage: (a) 2L inverter, (b) 3L inverter and (c) details of one of the six main triangles and sub-triangle (I-3b).

$$\begin{cases} u_\alpha = \frac{v_\alpha}{V_{dc}} = m \cos \vartheta, & u_\beta = \frac{v_\beta}{V_{dc}} = m \sin \vartheta & \text{for } 2L \\ u'_\alpha = \frac{v'_\alpha}{V_{dc}} = m \cos \vartheta, & u'_\beta = \frac{v'_\beta}{V_{dc}} = m \sin \vartheta & \text{for } 3L \end{cases} \quad (2)$$

being  $\alpha$  and  $\beta$  the indexes for real and imaginary components of  $\mathbf{v}^*$ , as represented in Figs. 1a and 1c. The calculation of the duty-cycles could be easily extended to the other sectors for 2L, 3L and ML inverters [2], [7]-[8].

In centered space vector PWM of 2L and ML inverters the application time of pivot vector ( $\delta_0$  or  $\delta_p$ ) is shared in equal parts for the two redundant pivot states. In this way, a nearly-optimal modulation, able to minimize the RMS of current ripple, is obtained [4], [11]. Considering CB-PWM, an equivalent switching pattern can be achieved by injecting a proper common-mode signal to the reference voltage waveforms. In this way, the resulting modulating signals are able to equally share the application times of redundant states. While for 2L inverters a simple min/max injection can be used for centering [2], a more complex common-mode signal has to be added to reference voltages in case of ML inverters [9]-[12]. A simplified procedure to obtain the centered optimized modulating signals has been recently introduced in [13] for the 3L case.

In this paper the ripple analysis is developed for centered space vector modulation, implemented by carried-based PWM, being one of the most popular 2L and ML modulations. In particular, CB-PWM offers inherent simplicity, flexibility, reduced computational time, and easy implementation on industrial DSPs, without the need of FPGA or any other additional hardware.

### III. PEAK-TO-PEAK CURRENT RIPPLE EVALUATION

Due to the symmetry among the three phases in the considered case of sinusoidal balanced currents, only the 1<sup>st</sup> phase is examined in the following analysis. The current ripple definition introduced in [17] is recalled here for better understanding. The basic equation for a RLE circuit, representing both motor-load and grid-connected systems, is

$$v(t) = Ri(t) + L \frac{di}{dt} + v_g(t). \quad (3)$$

Averaging (3) and introducing the current variation  $\Delta i = i(T_s) - i(0)$  in the switching period  $T_s$  gives

$$\bar{v}(T_s) = R\bar{i}(T_s) + L \frac{\Delta i}{T_s} + \bar{v}_g(T_s). \quad (4)$$

The alternating voltage  $\tilde{v}(t)$  is defined as the difference between instantaneous and average voltage components as

$$\tilde{v}(t) = v(t) - \bar{v}(T_s). \quad (5)$$

The instantaneous current ripple can be calculated by substituting (3) and (4) in (5), and integrating

$$\tilde{i}(t) = \Delta i(t) - \frac{t}{T_s} \Delta i \cong \frac{1}{L} \int_0^t \tilde{v}(t) dt. \quad (6)$$

This procedure is discussed with more details in [17]-[19].

Note that the current ripple calculated by (6) corresponds to the difference between the instantaneous current and its fundamental component.

The peak-to-peak current ripple amplitude is defined as the range of (6) in the switching period

$$\tilde{i}_{pp} = \max\{\tilde{i}(t)\}_0^{T_s} - \min\{\tilde{i}(t)\}_0^{T_s}. \quad (7)$$

In terms of space vectors, the variables of the 1<sup>st</sup> phase are given by the projection of the corresponding space vectors on the real axis. In particular, if the reference voltage is within the modulation limits, *i.e.*, the reference space vector  $\mathbf{v}^*$  lies within the outer hexagon, the average output voltage is given by

$$\bar{v}(T_s) = v^* = \text{Re}\{\mathbf{v}^*\} = V^* \cos \vartheta = V_{dc} m \cos \vartheta. \quad (8)$$

The instantaneous output voltage of the 1<sup>st</sup> phase can be expressed by switching states defined in (1), leading to

$$v(t) = V_{dc} \left[ S_1 - \frac{1}{3}(S_1 + S_2 + S_3) \right]. \quad (9)$$

The alternating voltage component for 2L and ML inverters can be determined by introducing (8) and (9) in (5):

$$\tilde{v}(t) = V_{dc} \left[ S_1 - \frac{1}{3}(S_1 + S_2 + S_3) \right] - m V_{dc} \cos \vartheta. \quad (10)$$

In order to evaluate the current ripple for both 2L and 3L inverters, only the three cases identified by the three different colored areas in Fig. 2 can be separately considered. The results are readily extended to the whole hexagons by exploiting the quarter-wave symmetry.

The analytical developments for ML inverters can be carried out by considering the residual reference voltage  $\mathbf{v}_{2L}$  instead of the original reference voltage  $\mathbf{v}^*$ , for each pivot vector  $\mathbf{v}_p$ , as emphasized by the pink colored regions in Fig. 1.

#### A. Evaluation for the two-level inverter

The ripple evaluation in the case of 2L inverter is summarized here since it is the basis of the proposed analysis for ML inverters. Considering 2L inverter, two different cases can be distinguished in sector I:  $0 \leq m \cos \vartheta \leq 1/3$  and  $m \cos \vartheta \geq 1/3$ , and one single case for the half of the sector II, corresponding to the three colored areas in Fig. 2.

The sub-case  $0 \leq m \cos \vartheta \leq 1/3$ , corresponding to the blue area of sector I in Fig. 2, is shown in diagram ❶ of Fig. 3a. In

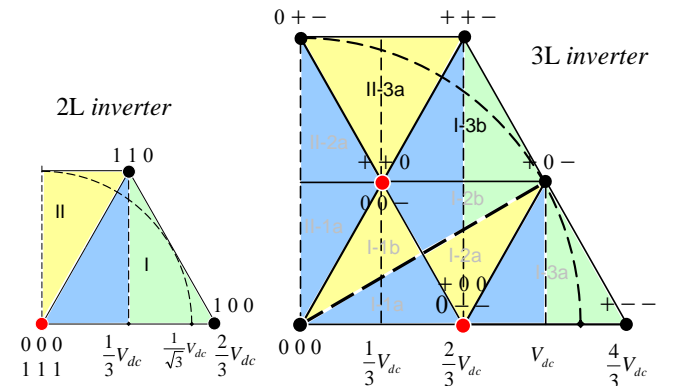


Fig. 2. 2L and 3L inverters voltage diagrams in the 1<sup>st</sup> quadrant of  $\alpha$ - $\beta$  plane.

particular, the current ripple and its peak-to-peak value are depicted, together with the instantaneous output voltage  $v(t)$ . In this case,  $\tilde{i}_{pp}$  can be evaluated by (6), (7) and (10), considering either switch configuration {111} or {000}, and the corresponding application time  $t_0/2$ , *i.e.*, duty-cycle  $\delta_0/2$ , according to Fig. 3a. Normalizing by (2) gives

$$\tilde{i}_{pp} = \frac{V_{dc}T_s}{2L} \{m \cos \vartheta \delta_0\} = \frac{V_{dc}T_s}{2L} \{u_\alpha \delta_0\}. \quad (11)$$

Peak-to-peak current ripple can also be expressed as

$$\tilde{i}_{pp} = \frac{V_{dc}T_s}{2L} r(m, \vartheta), \quad (12)$$

being  $r(m, \vartheta)$  the normalized peak-to-peak current ripple amplitude. Introducing in (11) the expression of  $\delta_0$  given in Table I, the normalized current ripple becomes

$$r(m, \vartheta) = u_\alpha \left[ 1 - \frac{3}{2} \left( u_\alpha + \frac{1}{\sqrt{3}} u_\beta \right) \right]. \quad (13)$$

The sub-case  $1/3 \leq m \cos \vartheta \leq 1/\sqrt{3}$ , corresponding to the green area of sector I in Fig. 2, is depicted in diagram ② of Fig. 3a. In this case  $\tilde{i}_{pp}$  can be evaluated considering both the switch configurations {111} and {110} with the corresponding duty-cycles  $\delta_0/2$  and  $\delta_2$ . Normalizing by (2) gives

$$\tilde{i}_{pp} = \frac{V_{dc}T_s}{2L} \left\{ u_\alpha \delta_0 + 2 \left( u_\alpha - \frac{1}{3} \right) \delta_2 \right\}. \quad (14)$$

Introducing in (14) the expression of  $\delta_0$  and  $\delta_2$  given in Table I, the normalized current ripple becomes

$$r(m, \vartheta) = u_\alpha \left[ 1 - \frac{3}{2} \left( u_\alpha + \frac{1}{\sqrt{3}} u_\beta \right) \right] + 2\sqrt{3} u_\beta \left( u_\alpha - \frac{1}{3} \right). \quad (15)$$

The only sub-case of the half of sector II, corresponding to the yellow area in Fig. 2, is depicted in Fig. 3a (right-hand side). In this case,  $\tilde{i}_{pp}$  can be evaluated considering both the switch configurations {000} and {010} with the corresponding duty-cycles  $\delta_0/2$  and  $\delta_2$ . Normalizing by (2) gives

$$\tilde{i}_{pp} = \frac{V_{dc}T_s}{2L} \left\{ u_\alpha \delta_0 + 2 \left( u_\alpha + \frac{1}{3} \right) \delta_2 \right\}. \quad (16)$$

Substituting in (16) the expression of  $\delta_0$  and  $\delta_2$  given in Table I for sector II, the normalized current ripple becomes

$$r(m, \vartheta) = u_\alpha \left[ 1 - \sqrt{3} u_\beta \right] + 3 \left( \frac{1}{\sqrt{3}} u_\beta - u_\alpha \right) \left( u_\alpha + \frac{1}{3} \right). \quad (17)$$

The analysis can be easily extended to all the other sectors of the 2L hexagon by exploiting the quarter-wave symmetry.

### B. Evaluation for the three-level inverter

Two different ways to analyze the current ripple in 3L inverter are presented in this sub-section. The first is based on the results of the 2L case introduced in the previous sub-section, resulting in a simpler and more general analysis. The alternative method is based on the direct analysis of 3L voltage waveforms, leading to more involved calculations and used here just to verify the results in the considered cases.

The ripple analysis in case of more than two levels can be carried out by taking into account that in each pivot sector the role of the pivot vector is similar to the role of the null vector in 2L inverter, according to the pink areas emphasized in Fig. 1 in case of 3L inverter. Considering the vector composition represented in Fig. 1c, the normalized reference voltages of 3L inverter can be written as

$$u'_\alpha = u_\alpha + 1/3, \quad u'_\beta = u_\beta + 1/\sqrt{3}, \quad (18)$$

where  $u_\alpha$  and  $u_\beta$  are the normalized reference voltages corresponding to the 2L inverter. From (18) the expressions of the 2L reference voltages can be derived as

$$u_\alpha = u'_\alpha - 1/3, \quad u_\beta = u'_\beta - 1/\sqrt{3}. \quad (19)$$

The sub-case  $m \cos \vartheta \leq 2/3$ , related to the blue area of triangle I-3b in Fig. 2, corresponds to the blue area of sector I in 2L inverter.  $\tilde{i}_{pp}$  can be evaluated introducing (19) in the expression obtained for 2L inverter (11), leading to

$$\tilde{i}_{pp} = \frac{V_{dc}T_s}{2L} \left\{ \left[ u'_\alpha - \frac{1}{3} \right] \delta_0 \right\}, \quad (20)$$

where  $\delta_0$  can be obtained by introducing (19) in the expression of duty-cycle of 2L inverter given in Table I. The normalized current ripple for 3L inverter becomes

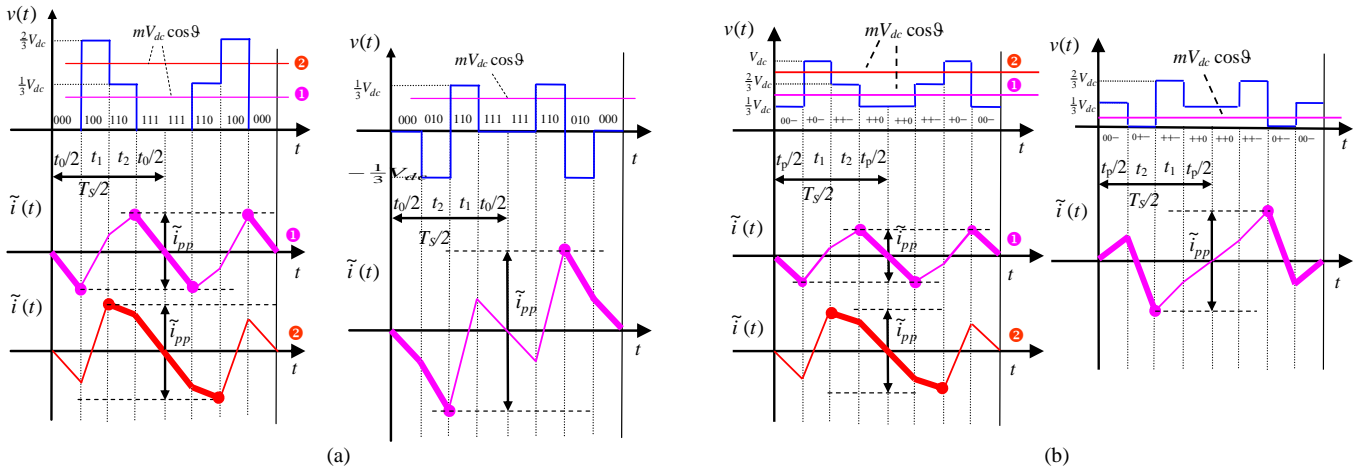


Fig. 3. Output voltage and current ripple in one switching period (a) for 2L inverter, sectors I and II, and (b) for 3L inverter, triangles I-3b and II-3a.

$$r(m, \vartheta) = \left(u'_\alpha - \frac{1}{3}\right) \left[ 1 - \frac{3}{2} \left( \left(u'_\alpha - \frac{1}{3}\right) + \frac{1}{\sqrt{3}} \left(u'_\beta - \frac{1}{\sqrt{3}}\right) \right) \right] = \left(u'_\alpha - \frac{1}{3}\right) \left[ 2 - \frac{3}{2} \left(u'_\alpha + \frac{1}{\sqrt{3}} u'_\beta\right) \right] \quad (22)$$

An alternative method to derive the peak-to-peak ripple amplitude for 3L inverter is to analyze the output voltage waveforms, as done for 2L inverter. The considered sub-case corresponding to the blue area of triangle I-3b in Fig. 2 is depicted in diagram ① of Fig. 3b. In this case,  $\tilde{i}_{pp}$  can be evaluated by (6), (7), and (10), considering the switch configuration  $\{++0\}$  or  $\{00-\}$ , according to Fig. 3b, with the corresponding duty-cycle  $\delta_p/2$ , leading to

$$\tilde{i}_{pp} = \frac{V_{dc} T_s}{2L} \left\{ \left(m \cos \vartheta - \frac{1}{3}\right) \delta_p \right\} = \frac{V_{dc} T_s}{2L} \left\{ \left(u'_\alpha - \frac{1}{3}\right) \delta_p \right\}. \quad (23)$$

After introducing the expression for  $\delta_p$  given in Table I for 3L inverter and normalization, the current ripple becomes

$$r(m, \vartheta) = \left(u'_\alpha - \frac{1}{3}\right) \left[ 2 - \frac{3}{2} \left(u'_\alpha + \frac{1}{\sqrt{3}} u'_\beta\right) \right]. \quad (24)$$

Comparing (24) with the expression (22) obtained with the analysis based on the 2L inverter, the matching is verified.

The sub-case  $m \cos \vartheta > 2/3$ , related to the green area of triangle I-3b in Fig. 2, corresponds to the green area of sector I in 2L inverter. Starting from the expression derived for the 2L inverter (14), and introducing (19), the peak-to-peak current ripple can be written as

$$\tilde{i}_{pp} = \frac{V_{dc} T_s}{2L} \left\{ \left(u'_\alpha - \frac{1}{3}\right) \delta_0 + 2 \left[ \left(u'_\alpha - \frac{1}{3}\right) - \frac{1}{3} \right] \delta_2 \right\}. \quad (25)$$

where  $\delta_0$  and  $\delta_2$  are the duty-cycles of 3L inverter obtained by substituting (19) in the expressions of duty-cycles of 2L inverter given in Table I. The normalized current ripple for 3L inverter becomes

$$r(m, \vartheta) = \left(u'_\alpha - \frac{1}{3}\right) \left[ 2 - \frac{3}{2} \left(u'_\alpha + \frac{1}{\sqrt{3}} u'_\beta\right) \right] + 2 \left(u'_\alpha - \frac{2}{3}\right) (\sqrt{3} u'_\beta - 1). \quad (26)$$

As in the previous case, peak-to-peak ripple amplitude can also be obtained by directly analyzing the output voltage waveforms. The considered sub-case, representing the green

area of triangle I-3b in Fig. 2, is depicted in diagram ② of Fig. 3b. In this case  $\tilde{i}_{pp}$  can be evaluated considering the switch configurations  $\{++0\}$  and  $\{+-\}$  and the corresponding duty-cycles  $\delta_p/2$  and  $\delta_2$ , leading to

$$\tilde{i}_{pp} = \frac{V_{dc} T_s}{2L} \left\{ \left(m \cos \vartheta - \frac{1}{3}\right) \delta_p + 2 \left(m \cos \vartheta - \frac{2}{3}\right) \delta_2 \right\}. \quad (27)$$

After introducing the expressions for  $\delta_p$  and  $\delta_2$  given in Table I for 3L inverter and normalization, current ripple becomes

$$r(m, \vartheta) = \left(u'_\alpha - \frac{1}{3}\right) \left[ 2 - \frac{3}{2} \left(u'_\alpha + \frac{1}{\sqrt{3}} u'_\beta\right) \right] + 2 \left(u'_\alpha - \frac{2}{3}\right) (\sqrt{3} u'_\beta - 1). \quad (28)$$

Comparing (28) with the expression (26) obtained with the analysis based on 2L inverter, the matching is verified.

The sub-case related to the yellow area of the half triangle II-3a in Fig. 2 corresponds to the yellow area of the half of sector II in 2L inverter. In this case  $\tilde{i}_{pp}$  can be evaluated by substituting (19) in the expression obtained for 2L inverter (16), leading to

$$\tilde{i}_{pp} = \frac{V_{dc} T_s}{2L} \left\{ \left(u'_\alpha - \frac{1}{3}\right) \delta_0 + 2 \left[ \left(u'_\alpha - \frac{1}{3}\right) + \frac{1}{3} \right] \delta_2 \right\}, \quad (29)$$

where  $\delta_0$  and  $\delta_2$  can be obtained by introducing (19) in the expressions of duty-cycles of 2L inverter given in Table I. The normalized current ripple for 3L inverter becomes

$$r(m, \vartheta) = \left(u'_\alpha - \frac{1}{3}\right) \left( 2 - \sqrt{3} u'_\beta \right) + 3 u'_\alpha \left( \frac{1}{\sqrt{3}} u'_\beta - u'_\alpha \right). \quad (30)$$

As in the previous cases, peak-to-peak ripple amplitude can also be obtained by directly analyzing the output voltage waveforms. The considered sub-case is depicted Fig. 3b (right-hand side). In this case  $\tilde{i}_{pp}$  can be evaluated considering the switch configurations  $\{++0\}$  and  $\{0+-\}$  and the corresponding duty-cycles  $\delta_p/2$  and  $\delta_2$ , leading to

$$\tilde{i}_{pp} = \frac{V_{dc} T_s}{2L} \left\{ \left(m \cos \vartheta - \frac{1}{3}\right) \delta_p + 2 m \cos \vartheta \delta_2 \right\}. \quad (31)$$

After introducing the expressions of  $\delta_p$  and  $\delta_2$  given in Table I for 3L inverter and normalization, current ripple becomes

$$r(m, \vartheta) = \left(u'_\alpha - \frac{1}{3}\right) \left( 2 - \sqrt{3} u'_\beta \right) + 3 u'_\alpha \left( \frac{1}{\sqrt{3}} u'_\beta - u'_\alpha \right). \quad (32)$$

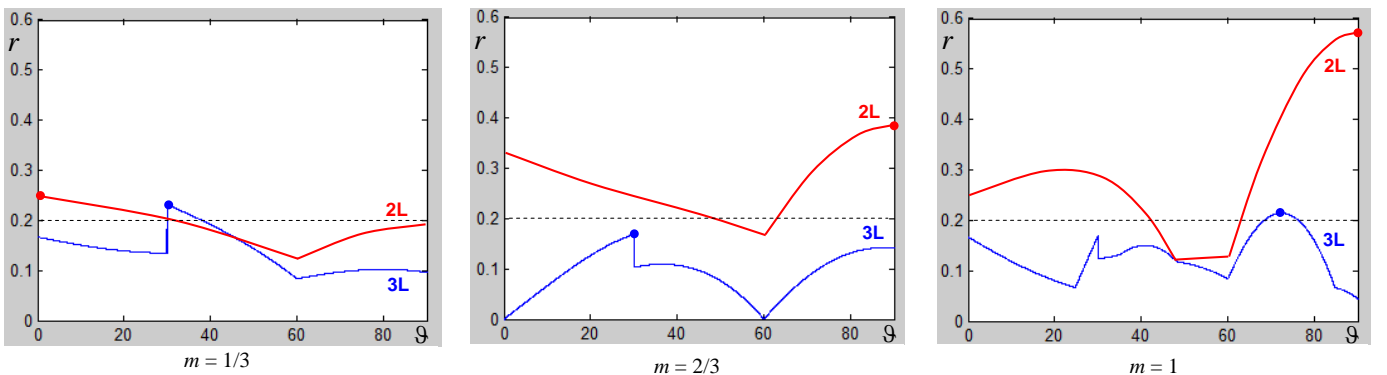


Fig. 4. Normalized peak-to-peak current ripple amplitude  $r(m, \vartheta)$  for 2L and 3L inverters in the range  $\vartheta = [0, 90^\circ]$  for different modulation indexes.

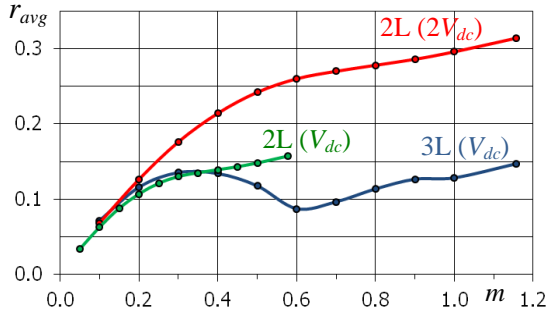


Fig. 5. Average normalized current ripple vs. modulation index.

Comparing (32) with the expression (30) obtained with the analysis based on 2L inverter, the matching is verified.

The analysis can be easily extended to the entire considered pivot sector and to all the other pivot sectors of 3L inverter by exploiting the quarter-wave symmetry (corresponding colored areas in Fig. 2). Moreover, by exploiting the algorithm proposed here, *i.e.* the calculation of the ripple for 3L inverters on the basis of the ripple in 2L inverters, the analysis can be easily extended to the general case of ML inverters. This is in contrast to extension of the direct method which is leading to more involved calculations.

### C. Ripple comparison between 2L and 3L inverter

In order to show and compare the behavior of the peak-to-peak current ripple amplitude in the fundamental period, the same output voltage range for 2L and 3L inverters should be considered. For this reason, the 2L inverter is supplied by double dc voltage,  $2V_{dc}$ , *i.e.*, all the derived ripple expressions are multiplied by 2, whereas each cell of the 3L inverter is supplied by  $V_{dc}$ . With this assumption, the modulation index is  $0 \leq m \leq 2/\sqrt{3}$  for both 2L and 3L inverters.

In Fig. 4 the normalized function  $r(m, \vartheta)$  defined by (12) for  $m = 1/3, 2/3, \text{ and } 1$ , is shown in case of 2L and 3L inverters. As expected, the ripple in 3L inverter is lower than the ripple of 2L inverter almost for the whole phase angle range. In the same figure, the maximum normalized current ripple ( $r^{max}$ ) is emphasized with dots. It is noted that  $r^{max}$  has a reduced variability with  $m$ , almost close to the value 0.2 (dashed line) in case of 3L inverter, whereas  $r^{max}$  is increasing almost proportionally with  $m$  in the case of 2L inverter [17]. This is due to the lower distance between the reference vector  $\mathbf{v}^*$  and the

available voltage vectors in the case of 3L inverter, exploited by applying the NTV modulation. The discontinuity noticed in the current ripple envelope of 3L inverter for  $\vartheta = 30^\circ$  is introduced by the pivot vector change, *i.e.* six times in the fundamental period. This discontinuity is easily recognizable in the modulating signals of centered carried-based PWM in the case of 3L inverters [11]-[13], whereas the modulating signals are continuous in the 2L case. Note that there is not discontinuity at  $\vartheta = \pm 90^\circ$  for the sake of the symmetry. A better view of this discontinuity from the point of view of space vectors is shown in the following colored map of current ripple.

In Fig. 5 the average of normalized current ripple,  $r_{avg}$ , is shown as a function of the modulation index to summarize the current ripple amplitude in the whole fundamental period. Three different cases are considered: 2L inverter supplied by  $V_{dc}$  and  $2V_{dc}$ , and 3L inverter supplied by  $V_{dc}$ . It can be noticed that 2L inverter supplied with  $2V_{dc}$  has almost the double of the average normalized ripple compared to 3L inverter, except for low modulation indexes, *i.e.* less than 0.4. The 2L inverter supplied with  $V_{dc}$  shows a lower ripple than 3L inverter for  $m < 1/3$ , whereas for  $m > 1/3$  up to the modulation limit of the 2L inverter ( $1/\sqrt{3}$ ), the ripple is lower for 3L inverter. The lower ripple in case of the 2L inverter for low modulation indexes (inner hexagon) can be explained with reference to the considered CB modulation. Namely, for 3L inverters the centered SV-PWM shares the pivot states into two equal parts and offers reduced harmonic distortion in the output currents. However, it is not the most optimal modulation within the inner hexagon (corresponding to the hexagon in 2L inverter), since the used pivot vectors are not the zero vector. The centered SV-PWM modulation in 2L inverter, which uses the zero vector as pivot vector is known to be the most optimal in this case.

Fig. 5 also shows that  $r_{avg}$  has a reduced excursion in the case of 3L inverter, oscillating between 0.075 and 0.15 for  $m = [0.1, 1]$ , whereas it is a monotonic increasing function of  $m$  ranging in a wider range in the case of 2L inverter. The average current ripple amplitude can be also used to compare the performance of 2L and 3L PWM inverters with current hysteresis controlled inverters, having a current ripple amplitude almost constant.

Fig. 6 shows the colored maps of  $r(m, \vartheta)$  in the 1<sup>st</sup> quadrant within the modulation limits for 2L and 3L inverters. The dis-

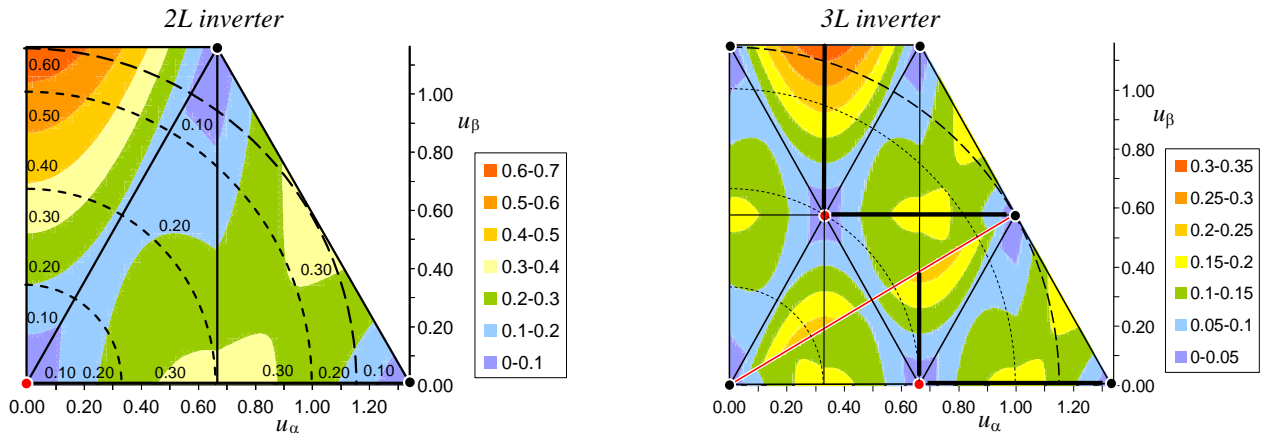


Fig. 6. Maps of the normalized peak-to-peak current ripple amplitude  $r(m, \vartheta)$  for 2L inverter (supplied by  $2V_{dc}$ ) and 3L inverter (supplied by  $V_{dc}$ ).

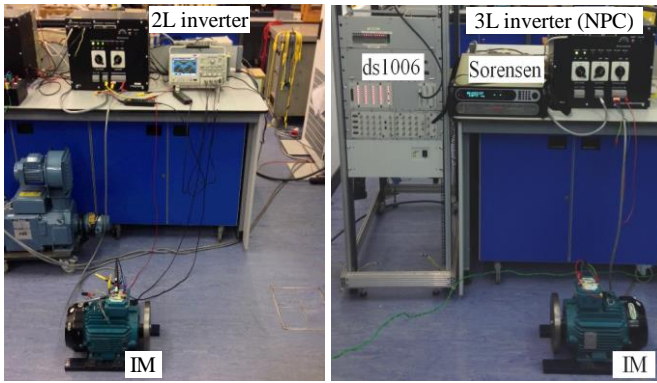


Fig. 7. Experimental setups of 2L and 3L inverters.

continuity of the ripple across the border of pivot sectors (red line) in 3L inverter is now well observed, due to the pivot vector change. Namely, the red line divides the two pivot sectors (one of pivot vector  $v_{p1}$ , and another of  $v_{p6}$ ). In the case of sub-triangles I-1a and I-2a, the pivot vector applied is  $v_{p6}$ , while in the case of the sub-triangles I-1b and I-2b the pivot vector is  $v_{p1}$ . Note that the pivot vector determines the sequence of applied voltage levels. As a consequence, also

within the same NTV, *i.e.* the same available voltage levels, a pivot change causes a different current ripple.

For both 2L and 3L inverters can be noted that ripple amplitude is going to zero in the surroundings of each output voltage vector, since the reference vector is almost perfectly synthesized and the alternating voltage (5) goes to zero. Even though in Fig. 6 are kept the same colors for both ripple maps, the color scale for 2L inverter is the double than for 3L inverter. The 1<sup>st</sup> quadrant ripple map of 2L inverter is emphasized with bold lines in ripple map of 3L inverter, for each pivot vector.

IV. RESULTS

In order to verify the analytical developments proposed in the previous sections, numerical simulations and corresponding experimental tests are carried out. Circuit simulations are performed by Sim-PowerSystems of Matlab considering both 2L and 3L inverters with ideal switches, *i.e.*, no dead-time was implemented in order to match perfectly the theoretical developments. Experimental tests are carried out by custom-made converters. In particular, the 2L inverter is implemented by In-

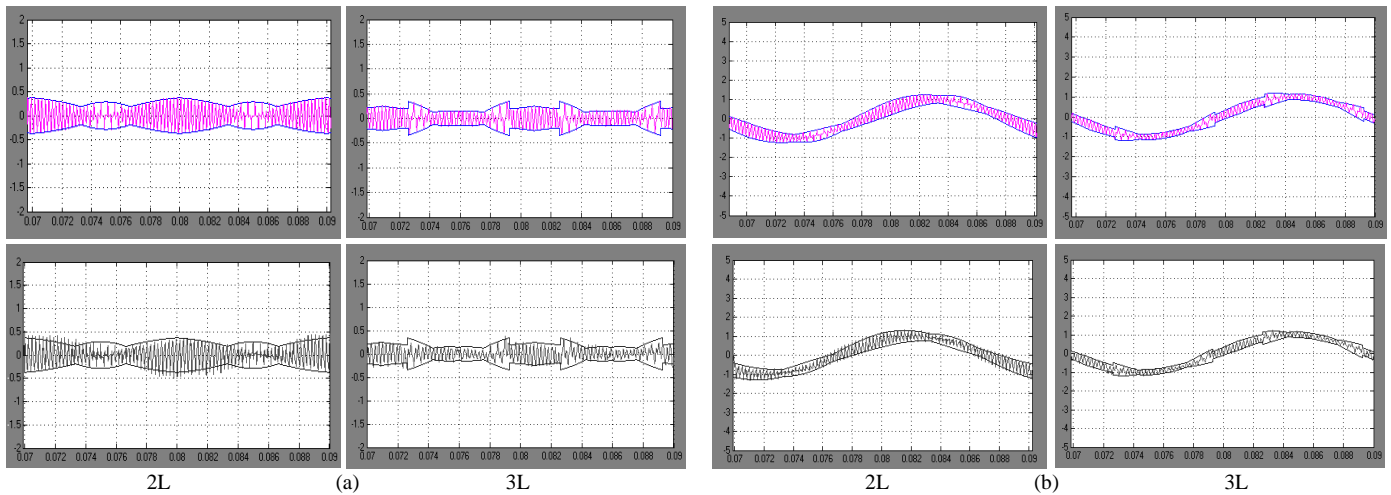


Fig. 8. Simulation (colored, top) and experimental (gray, bottom) results for 2L and 3L inverters,  $m = 1/3$ : (a) current ripple with calculated peak-to-peak amplitude, (b) instantaneous output current with calculated current envelopes.

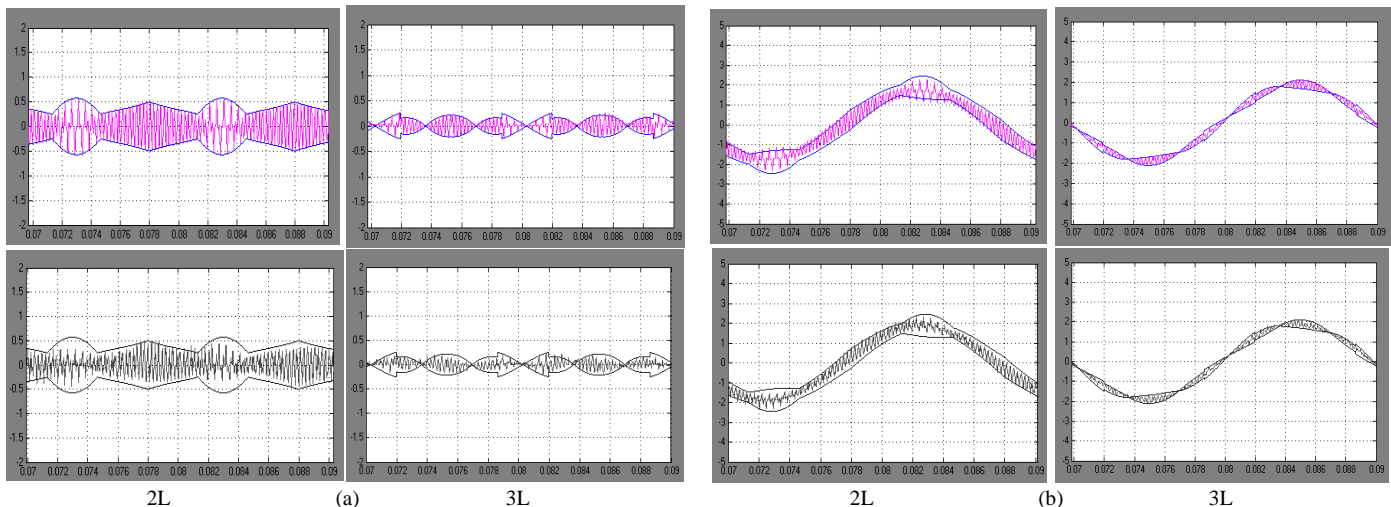


Fig. 9. Simulation (colored, top) and experimental (gray, bottom) results for 2L and 3L inverters,  $m = 2/3$ : (a) current ripple with calculated peak-to-peak amplitude, (b) instantaneous output current with calculated current envelopes.

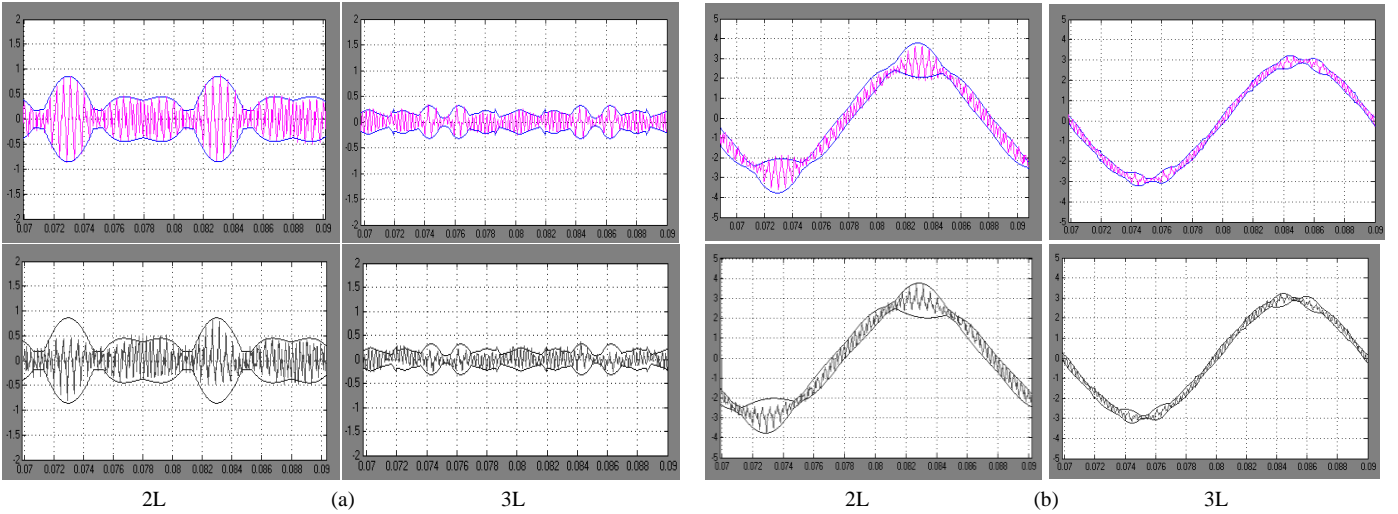


Fig. 10. Simulation (colored, top) and experimental (gray, bottom) results for 2L and 3L inverters,  $m = 1$ : (a) current ripple with calculated peak-to-peak amplitude, (b) instantaneous output current with calculated current envelopes.

fineon FS50R12KE3 IGBT pack, and the 3L inverter (NPC type) is implemented by Semikron SKM50GB12T4 IGBT modules, with Semikron SKKD 46/12 clamping diodes. The dSpace ds1006 hardware has been employed for the real-time implementation of algorithms. The experimental setups of 2L and 3L inverters are shown in Fig. 7.

In order to compare 2L and 3L inverters with the same output voltage capabilities, 600 V total dc voltage supply ( $2V_{dc}$ ) was provided from Sorensen SGI 600/25 for both inverters. With this assumption, analytical developments are carried out with  $V_{dc} = 300$  V and  $0 \leq m \leq 2/\sqrt{3}$  for both 2L and 3L inverters.

Switching frequency was set to 2.1 kHz and a dead-time of 6  $\mu$ s (not compensated) was implemented in the hardware. Fundamental frequency was kept at 50 Hz for easier comparison with analytical developments. The nearly-optimal centered carrier-based PWM is implemented leading to equally share the application times of pivot vectors.

For both 2L and 3L inverters the load was a three-phase induction motor (mechanically unloaded) having the following stator-referred parameters: stator resistance  $R_s = 2.4 \Omega$ , rotor resistance  $R_r' = 1.6 \Omega$ , stator leakage inductance  $L_{ls} = 12$  mH, rotor leakage inductance  $L_{lr}' = 12$  mH, magnetizing inductance  $L_m = 300$  mH, 2 pole pairs. According to the model of induction motor for higher order harmonics, which are determining the current ripple, the estimated total equivalent inductance  $L = L_{ls} + L_{lr}' = 24$  mH is considered for the ripple evaluation.

Tektronix oscilloscope MSO2014 with current probe TCP 0030 was used for measurements, and the built-in noise filter (cut-off frequency  $f_c = 600$  kHz) was applied. A further low-pass filter ( $f_c = 25$  kHz) was applied in post-processing of the experimental data to better clean the waveforms from the switching noise. The instantaneous current ripple is calculated as the difference between instantaneous and fundamental current components, according to (6)

$$\tilde{i}(t) = i(t) - i_{fund}(t). \quad (33)$$

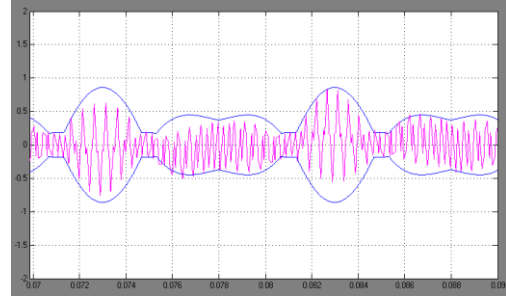


Fig. 11. Simulation results for 2L inverter,  $m = 1$ , accounting for dead-time and considering a slightly higher load inductance (+15%), (see Fig.10(a)).

As in the previous sections, the 1<sup>st</sup> phase is selected for further analysis and different values of  $m$  are investigated to cover the different sub-cases in the whole linear modulation index range.

Figs. 8, 9, and 10 show simulation and corresponding experimental results for  $m = 1/3, 2/3$ , and 1, respectively. In particular, for all figures, the upper diagrams show the simulation results (pink traces) and the calculated ripple envelopes (blue traces). The bottom diagrams show the corresponding experimental results (gray traces). Left and right diagrams are corresponding to 2L and 3L inverters with the same y-axis range for easier comparison. In Figs. 8a, 9a, and 10a the current ripple evaluated by (33) is depicted, whereas in Figs. 8b, 9b, and 10b the phase current is shown.

It can be noticed that simulation results perfectly match the calculated envelopes, for all the considered cases. Experimental results are also in a good agreement with the analytical developments, just a slightly lower current ripple can be observed. This small mismatch is more emphasized in the 2L case, for high modulation indexes. It has been verified that the main origin of the observed lower value lies in the inverter dead-time, being not compensated in the experimental implementation but not considered in both simulations and analytical developments. Furthermore, the load (motor) inductance has been probably slightly underestimated. In order to prove these considerations, additional simulations have been carried



out, introducing dead-time and slightly increasing the load inductance (+15%,  $\approx 28$  mH), showing a better matching with the experimental results. As an example, in Fig. 11 is shown the case  $m = 1$  for the 2L inverter, corresponding to Fig. 10 (a). It can be noticed that the effect of dead-time is to slightly reduce the current ripple, changing the envelope profile and causing an asymmetry of the positive and negative envelopes.

## V. CONCLUSION

This paper gives analysis and comparison of instantaneous output current ripple in three-phase 2L and 3L inverters. The peak-to-peak ripple evaluation in 2L inverter is performed by analyzing the output voltage waveforms. It is shown that ripple evaluation in 3L inverter can be carried out either as an extension of the analysis of the 2L inverter or by directly analyzing the 3L inverter output voltage waveform. The same procedure can be extended to the case of more than three levels.

Normalized peak-to-peak current ripple is introduced, and different ripple diagrams are given for 2L and 3L inverters making possible a comparison considering the same output voltage range or the same dc voltage supply. In particular, reference is made to centered SVM for both 2L and 3L inverters. Readable and effective ripple maps are introduced to emphasize the ripple distribution in the fundamental period for the whole voltage modulation range of 2L and 3L inverters. As expected, the comparison shows that the ripple in 3L inverter is generally lower than the ripple of 2L inverter in case of the same output voltage range.

The analytical developments have been verified with numerical simulations and corresponding experimental tests for various modulation indexes, showing a good matching.

## REFERENCES

- [1] D. Zhao, V.S.S. Pavan Kumar Hari, G. Narayanan, R. Ayyanar, "Space-vector-based hybrid pulsewidth modulation techniques for reduced harmonic distortion and switching loss," *IEEE Trans. Power Electron.*, vol. 25, no. 3, pp. 760–774, April 2010.
- [2] D. Holmes, T.A. Lipo, *Pulse Width Modulation for Power Converters - Principles and Practice*. IEEE Press Series on Power Engineering, John Wiley and Sons, Piscataway, NJ, USA, 2003, pp. 215–257.
- [3] J.W. Kolar, H. Ertl, F.C. Zach, "Minimizing the current harmonics RMS value of three-phase PWM converter systems by optimal and suboptimal transition between continuous and discontinuous modulation," in *Proc. of 22nd Annual IEEE Power Electron. Spec. Conf. (PESC)*, Cambridge, MA, 24–27 June 1991, pp. 372–381.
- [4] D. Casadei, G. Serra, A. Tani, L. Zarri, "Theoretical and Experimental Analysis for the RMS Current Ripple Minimization in Induction Motor Drives Controlled by SVM Technique," *IEEE Trans. Ind. Electron.*, vol. 51, no. 5, pp. 1056–1065, Oct. 2004.
- [5] X. Zhang, J. Spencer, "Study of multisampled multilevel inverters to improve control performance," *IEEE Trans. Power Electron.*, vol. 27, no. 11, pp. 4409–4416, June 2012.
- [6] B. Vafakhah, J. Salmon, A.M. Knight, "A New Space-Vector PWM With Optimal Switching Selection for Multilevel Coupled Inductor Inverters," *IEEE Trans. Ind. Electron.*, vol. 57, no. 7, pp. 2354–2364, June 2010.
- [7] M.M. Prats, J.M. Carrasco, L.G. Franquelo, "Effective algorithm for multilevel converters with very low computational cost," *IET Electronics Letters*, vol. 38, no. 22, pp. 1398–1400, Oct. 2002.
- [8] S. Wei, B. Wu, F. Li, C. Liu, "A General Space Vector PWM Control Algorithm for Multilevel Inverters," in *Proc. of 18th IEEE Annual Appl. Power Electron. Conf. and Expos. (APEC)*, Miami Beach (FL), 9–13 Feb. 2003, pp. 562–568.
- [9] Y.H. Lee, D.H. Kim, D.S. Hyun, "Carrier based SVPWM method for multi-level system with reduced HDF," in *Proc. of IEEE Industry Applications Conference*, Rome (IT), 8–12 Oct. 2000, pp. 1996–2003.
- [10] P.C. Loh, D.G. Holmes, Y. Fukuta, T.A. Lipo, "Reduced common-mode modulation strategies for cascaded multilevel inverters," *IEEE Trans. Ind. Appl.*, vol. 39, no. 5, pp. 1386–1395, Sept. 2003.
- [11] B.P. McGrath, D.G. Holmes, T.A. Lipo, "Optimized space vector switching sequences for multilevel inverters," *IEEE Trans. Power Electron.*, vol. 18, no. 6, pp. 1293–1301, Nov. 2003.
- [12] F. Wang, "Sine-triangle versus space-vector modulation for three-level PWM voltage-source inverters," *IEEE Trans. Ind. Appl.*, vol. 38, no. 2, pp. 500–506, March/April 2002.
- [13] G. Grandi, J. Loncarski, "Simplified implementation of optimised carrier-based PWM in three-level inverters," *IET Electronics Letters*, vol. 50, no. 8, pp. 631–633, 10 April 2014.
- [14] S. Srinivas, K. Ramachandra Sekhar, "Theoretical and experimental analysis for current in a dual-inverter-fed open-end winding induction motor drive with reduced switching PWM," *IEEE Trans. Ind. Electron.*, vol. 60, no. 10, pp. 4318–4328, Oct. 2013.
- [15] A. Ruderman, "Understanding PWM current ripple in star-connected AC motor drive," *IEEE Power Electronics Society Newsletter*, vol. 21, no. 2, pp. 14–17, 2<sup>nd</sup> quarter 2009.
- [16] D. Jiang, F. Wang, "Current-ripple prediction for three-phase PWM converters," *IEEE Trans. Ind. Appl.*, vol. 50, no. 1, pp. 531–538, Jan/Feb 2014.
- [17] G. Grandi, J. Loncarski, "Evaluation of current ripple amplitude in three-phase PWM voltage source inverters," in *Proc. of 8th IEEE Int. Conf. Workshop on Compatibility and Power Electron. (CPE)*, Ljubljana (SLO), 5–7 June 2013.
- [18] G. Grandi, J. Loncarski, "Evaluation of current ripple amplitude in five-phase PWM voltage source inverters," in *Proc. of IEEE Conf. on ICT, Power engineering, and Signal processing (EUROCON)*, Zagreb (CRO), 1–4 July 2013.
- [19] G. Grandi, J. Loncarski, "Analysis of Peak-to-Peak Current Ripple Amplitude in Seven-Phase PWM Voltage Source Inverters," *Energies*, vol. 6, ISSN 1996-1073, 2013.
- [20] G. Grandi, J. Loncarski, C. Rossi, "Comparison of Peak-to-Peak Current Ripple Amplitude in Multiphase PWM Voltage Source Inverters," in *Proc. of 15th IEEE Conf. on Power Electron. and Appl. (EPE'13 ECCE Europe)*, Lille (FR), 3–5 Sept. 2013.
- [21] D. Jiang, F. Wang, "A General Current Ripple Prediction Method for the Multiphase Voltage Source Converter," *IEEE Trans. Power Electron.*, vol. 29, no. 6, pp. 2643–2648, June 2014.
- [22] G. Grandi, J. Loncarski, R. Seebacher, "Effects of Current Ripple on Dead-Time Analysis of Three-Phase Inverters," in *Proc. of IEEE Energy Conf. (ENERGYCON)*, Florence (IT), 9–12 Sept. 2012, pp. 207–212.
- [23] C.N.M. Ho, V.S.P. Cheung, H.S.H. Chung, "Constant-frequency hysteresis current control of grid-connected VSI without bandwidth control," *IEEE Trans. Power Electron.*, vol. 24, no. 11, pp. 2484–2495, Nov. 2009.
- [24] D.G. Holmes, R. Davoodnezhad, B.P. McGrath, "An improved three-phase variable-band hysteresis current regulator," *IEEE Trans. Power Electron.*, vol. 28, no. 1, pp. 441–450, Jan. 2013.
- [25] A. Shukla, A. Ghosh, A. Joshi, "Hysteresis modulation of multilevel inverters," *IEEE Trans. Power Electron.*, vol. 26, no. 5, pp. 1396–1409, May 2011.
- [26] D. Jiang, F. Wang, "Variable switching frequency PWM for three-phase converters based on current ripple prediction," *IEEE Trans. Power Electron.*, vol. 28, no. 11, pp. 4951–4961, Nov. 2013.
- [27] J. H. Seo, C. H. Choi and D. S. Hyun, "A new simplified space-vector PWM method for three-level inverters," *IEEE Trans. Power Electron.*, vol. 16, no. 4, pp. 545–550, July 2001.



**Gabriele Grandi** (M'00–SM'13) received the M.Sc. (*cum laude*) and the Ph.D. degrees in Electrical Engineering from University of Bologna, Italy, in 1990 and 1994, respectively. He joined the Department of Electrical Engineering, University of Bologna, since 1995 as Research Associate and since 2005 as Associate Professor. In 2013 was qualified as full professor of Electrical Engineering. He has published more than 120 papers on conference proceedings and international journals. His main research interests are focused on power electronic circuits and photovoltaics.



**Jelena Loncarski** (S'11) received the Dipl. Ing. and M.Sc. degrees from the Faculty of Electrical Engineering, University of Belgrade, Serbia, in 2007 and 2010, respectively. She joined the Dept. of Electrical Engineering, University of Bologna, in January 2011 as a PhD student. Dr Loncarski received her PhD degree in March 2014. In April 2014 she joined the Department of Engineering Sciences, Ångström Laboratory, Uppsala University as a Post Doc. Her main research interests are focused on power electronic circuits

and power electronic converters for renewable energy sources.



**Obrad Dordevic** (S'11, M'13) received his Dipl. Ing. Degree in Electronic Engineering from the University of Belgrade, Serbia, in 2008. He joined Liverpool John Moores University in December 2009 as a PhD student. Dr Dordevic received his PhD degree in April 2013 and is now a Lecturer at the Liverpool John Moores University. His main research interests are in the areas of power electronics, electrostatic precipitators, and advanced variable speed drives.